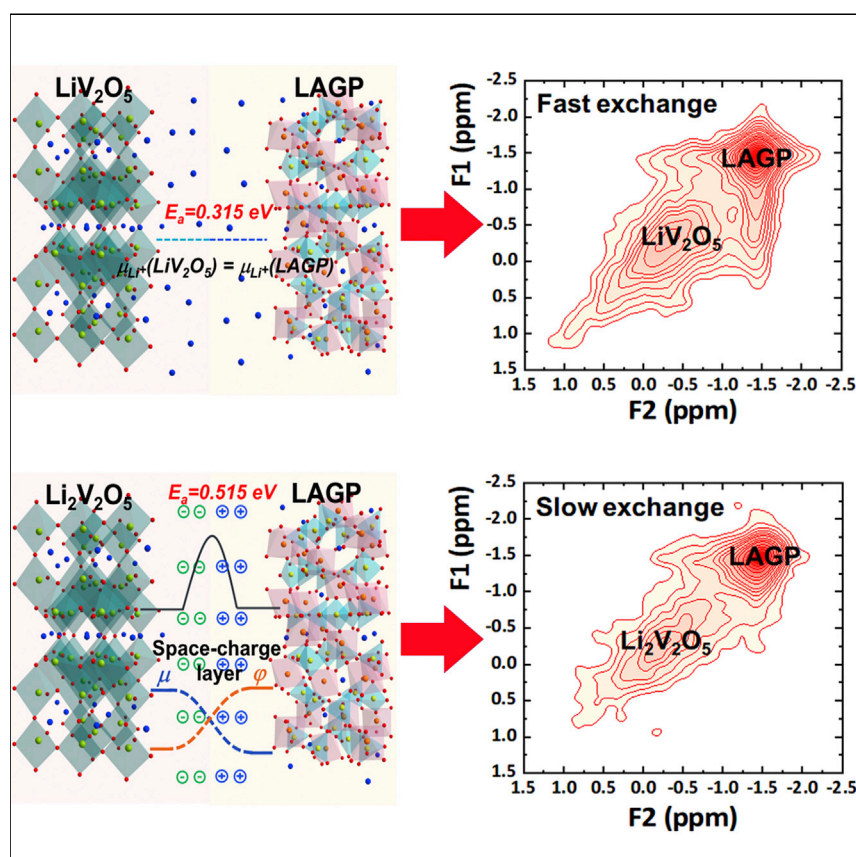


Article

Revealing the Impact of Space-Charge Layers on the Li-Ion Transport in All-Solid-State Batteries



Direct and quantitative measurement of the effect of space charges in solid-state batteries remains very challenging. Here, we reveal the effect on the Li-ion transport quantitatively by NMR 2D exchange experiments and space-charge layer model calculations on the $\text{Li}_x\text{V}_2\text{O}_5$ -LAGP interface. It is demonstrated that the space-charge layer leads to a higher barrier for Li-ion diffusion and smaller exchange current density and thus to a significantly higher interface resistance at the cathode-solid electrolyte interface.

Zhu Cheng, Ming Liu, Swapna Ganapathy, ..., Ping He, Haoshen Zhou, Marnix Wagemaker

pinghe@nju.edu.cn (P.H.)
hszhou@nju.edu.cn (H.Z.)
m.wagemaker@tudelft.nl (M.W.)

HIGHLIGHTS

The space-charge layer is controlled through the chemical potential of the electrode

NMR exchange selectively measures Li-ion transport over the space-charge layer

The barrier for Li-ion diffusion increases significantly due to the space-charge layer

Article

Revealing the Impact of Space-Charge Layers on the Li-Ion Transport in All-Solid-State Batteries

Zhu Cheng,¹ Ming Liu,² Swapna Ganapathy,² Chao Li,¹ Zhaolong Li,² Xiaoyu Zhang,¹ Ping He,^{1,*} Haoshen Zhou,^{1,3,*} and Marnix Wagemaker^{2,4,*}

SUMMARY

The influence of space-charge layers on the ionic charge transport over cathode-solid electrolyte interfaces in all-solid-state batteries remains unclear because of the difficulty to unravel it from other contributions to the ion transport over the interfaces. Here, we reveal the effect of the space-charge layers by systematically tuning the space-charge layer on and off between $\text{Li}_x\text{V}_2\text{O}_5$ and $\text{Li}_{1.5}\text{Al}_{0.5}\text{Ge}_{1.5}(\text{PO}_3)_4$ (LAGP), by changing the $\text{Li}_x\text{V}_2\text{O}_5$ potential and selectively measuring the ion transport over the interface by two-dimensional (2D) NMR exchange. The activation energy is demonstrated to be 0.315 eV for lithium-ion exchange over the space-charge-free interface, which increases dramatically to 0.515 eV for the interface with a space-charge layer. Comparison with a space-charge model indicates that the charge distribution due to the space-charge layer is responsible for the increased interface resistance. Thereby, the present work provides selective and quantitative insight into the effect of space-charge layers over electrode-electrolyte interfaces on ionic transport.

INTRODUCTION

Lithium (Li) batteries are gaining an ever-increasing attention due to the huge demand for high energy density and high-safety electrical energy storage and conversion devices.^{1–3} However, commercial Li-ion batteries suffer from severe safety problems associated with the flammable liquid electrolytes.^{4,5} All-solid-state batteries (ASSBs) are considered to be an effective solution to these concerns,⁶ and, in addition to being safer, ASSBs also possess additional advantages, such as higher practical energy densities and less stringent packaging demands.⁷ Although massive research efforts were invested in ASSBs over the last few years, facile Li-ion transport within the ASSBs remains a grand challenge, hindering market application of the ASSBs.^{8–10} Over the last few years, a number of solid-state electrolytes have been discovered with unexpectedly high ionic conductivities in the range of 10^{-3} – 10^{-2} S cm⁻¹, which means that the bulk ionic conductivity of solid-state electrolytes is no longer a major concern.^{11–13} Currently, the solid-solid interface between the electrode and solid-state electrolyte presents the largest challenges. First, the small effective interface area between the solid electrolyte and electrode can lead to a large barrier for charge transfer. Second, ion transport may be challenged by electrochemical decomposition reactions of the solid electrolyte in combination with the electrode, leading to poorly Li-ion conducting interphases.^{14,15} Third, the volumetric changes associated with the decomposition reactions, as well as the reversible ion storage in the electrodes, can lead to contact loss.^{16,17} Finally, the space-charge layer, the formation of electrochemical double layers

Context & Scale

All-solid-state batteries attract great attention because of their intrinsic safety and high energy density. However, the solid electrolyte-electrode interfaces pose several challenges toward the required Li-ion transport. One of the most difficult processes to expose is the influence of space charges at the electrode-solid electrolyte interface, and thus its effect on battery performance remains unclear. Here, we quantitatively reveal the Li-ion transport over the space-charge layer by 2D NMR exchange experiments, demonstrating that the activation energy for Li-ion exchange increases significantly because of the presence of the space-charge layer, lowering the exchange current density and raising the internal resistance. This work points out the importance to mitigate space-charge layers at the cathode-solid electrolyte interfaces to improve the charge transport in all-solid-state batteries.

at the solid-solid electrode-electrolyte interfaces typically results in local charge carrier depletion or enrichment, which in turn may influence the charge transport.^{15,18–20} The space-charge layer can enhance the ionic condition in solid-solid dispersions having intrinsic poor bulk ionic conductivity,^{21–24} but for solid electrolytes, that are designed to have a high conductivity, it is expected to be detrimental for ion transport by creating an interface barrier for Li-ion transport.^{25,26} However, the impact of space charges on the charge transport is very unclear, as demonstrated by the very different results reported,^{27–29} which can mainly be ascribed to the difficulty to observe the Li-ion distributions at the interfaces on the atomic scale and many material aspects as well as electrochemical conditions that influence the interface properties.

The present work aims at quantifying and understanding the impact of space-charge layers on the Li-ion migration across the solid-solid cathode-electrolyte interface by systematically varying the space charge by controlling the Li-chemical potential of the electrode material. Specifically the LAGP- $\text{Li}_x\text{V}_2\text{O}_5$ interface is investigated where the chemical potential of Li in the $\text{Li}_x\text{V}_2\text{O}_5$ ^{30–32} electrode can be controlled by the composition between 2 and 4 V versus Li/Li⁺ by means of the solid solution reaction, rationalizing the selection of the active material. Specifically, the LiV_2O_5 , $\text{Li}_2\text{V}_2\text{O}_5$, and $\text{Li}_{0.2}\text{V}_2\text{O}_5$ compositions are prepared by chemical lithiation, having the same, a lower, and a higher Li-chemical potential, respectively, as compared with that in LAGP. In this way, the space-charge layer at the LAGP- $\text{Li}_x\text{V}_2\text{O}_5$ interface will be switched off for LiV_2O_5 and switched on for $\text{Li}_{0.2}\text{V}_2\text{O}_5$ and $\text{Li}_2\text{V}_2\text{O}_5$, albeit with reversed polarity. As the potential range of $\text{Li}_x\text{V}_2\text{O}_5$ falls within the expected electrochemical stability of LAGP,³³ a stable interface between LAGP and $\text{Li}_x\text{V}_2\text{O}_5$ is expected, thereby exposing the impact of the space-charge layer. To measure the Li-ion equilibrium transport over these interfaces, we employed two-dimension exchange NMR spectroscopy (2D-EXSY), a powerful method to investigate the Li-ion transport over the interfaces.^{34–36} These experiments show that switching on the space-charge layer leads to a significant increase in the activation energy for Li-ion diffusion over the LAGP- $\text{Li}_2\text{V}_2\text{O}_5$ interface, in agreement with a 4-fold increase in resistance calculated with space-charge layer model. Thereby, direct evidence of the impact of space-charge layer on the Li-ion transport over the solid electrolyte-electrode interfaces is provided, which demonstrates that it can contribute significantly to the internal resistance. These insights motivate to develop rational interface strategies to reduce the space-charge layer effect in ASSBs in order to improve the ASSBs performance, for instance through reducing the local chemical potential differences at the electrode-electrolyte interfaces.

RESULTS AND DISCUSSION

Equilibrium Potential of LAGP and $\text{Li}_x\text{V}_2\text{O}_5$

The diffraction peaks of the prepared LAGP material in Figure S1A can be indexed with the NASICON $\text{LiGe}_2(\text{PO}_4)_3$ structure, indicating the successful synthesis of LAGP. The average crystallite size of LAGP is 110 nm, as derived from X-ray diffraction (XRD) line broadening. The LAGP pellet was coated with Au on both sides for the impedance measurements. From the fitting result of Figure S1B, the calculated ionic conductivity of the as prepared LAGP is 0.12 mS cm^{-1} , consistent with previously reported values,³⁷ demonstrating the high ionic conductivity. Although LAGP is considered to be a quite stable solid-state electrolyte, a small amount of Li can still be extracted from its crystal structure by electrochemical charging at small current densities.³⁸ LAGP was used as cathode material to assemble a LAGP/Li-metal cell, of which the galvanostatic intermittent titration technique (GITT) measurement, repeatedly 30 min charging at $5 \mu\text{A cm}^{-1}$ and 8 h resting, is shown in Figure 1A.

¹Center of Energy Storage Materials & Technology, College of Engineering and Applied Sciences, Jiangsu Key Laboratory of Artificial Functional Materials, National Laboratory of Solid State Microstructures, Collaborative Innovation Center of Advanced Microstructures, Nanjing University, Nanjing 210093, China

²Section Storage of Electrochemical Energy, Radiation Science and Technology, Faculty of Applied Sciences, Delft University of Technology, Delft 2629 JB, the Netherlands

³Energy Technology Research Institute, National Institute of Advanced Industrial Science and Technology (AIST), 1-1-1, Umezono, Tsukuba 305-8568, Japan

⁴Lead Contact

*Correspondence: pinghe@nju.edu.cn (P.H.), hszhou@nju.edu.cn (H.Z.), m.wagemaker@tudelft.nl (M.W.)

<https://doi.org/10.1016/j.joule.2020.04.002>

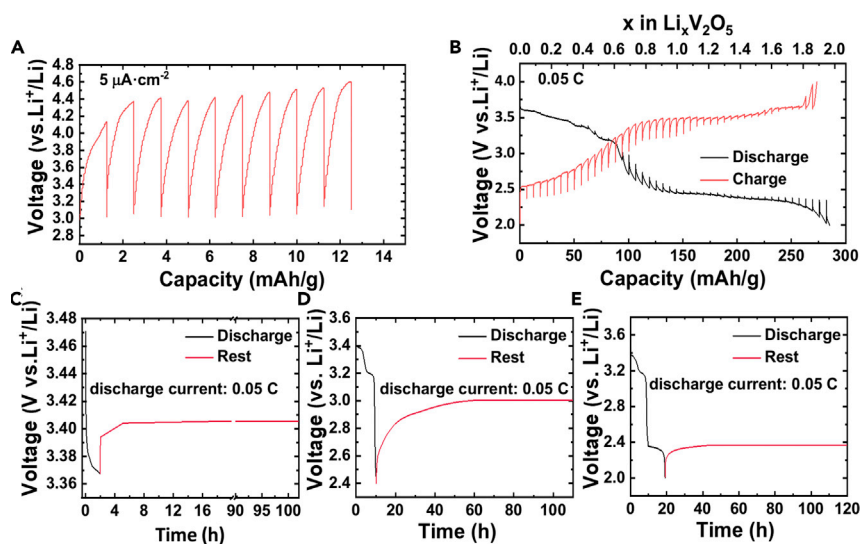


Figure 1. Determination of Equilibrium Potential of LAGP and $\text{Li}_x\text{V}_2\text{O}_5$ by GITT Measurements

Both GITT measurements were set as charging and discharging for 30 min and 8 h rest. The LAGP/Li cell was charged at a current density of $5 \mu\text{A}\cdot\text{cm}^{-2}$. The $\text{V}_2\text{O}_5/\text{Li}$ cell was charged and discharged at 0.05 C.

(A) GITT measurements of LAGP/Li cells.

(B) GITT measurements of $\text{V}_2\text{O}_5/\text{Li}$ cells.

(C–E) Discharging $\text{V}_2\text{O}_5/\text{Li}$ cell at 0.05 C for (C) 2 h, (D) 10 h, and (E) 20 h, respectively, then resting it for 100 h.

The cut-off voltage of this GITT measurement was set to 4.6 V to avoid electrolyte decomposition at higher potentials. After the first charging and rest step, the voltage of LAGP/Li cell returned to 3 V, as demonstrated in Figure 1A, which implies that the equilibrium potential of LAGP is around 3 V (the extracted Li content in the first charging process is negligible considering a small current density of $5 \mu\text{A}\cdot\text{cm}^{-1}$). GITT measurements were also conducted on the $\text{V}_2\text{O}_5/\text{Li}$ cells to determine the relationship between the composition and the equilibrium potential. In Figure 1B, the GITT curve shows the typical $\text{Li}_x\text{V}_2\text{O}_5$ electrochemical behavior with a gradual decreasing voltage between 3.6 and 2.4 V versus Li/Li^+ , representing a solid solution reaction, and a plateau around 2.4 V, representing a first order phase transition.³⁹ This demonstrates that the equilibrium potential of $\text{Li}_x\text{V}_2\text{O}_5$ can be adjusted between 2.4 to 3.6 V by tuning the composition between $0 < x < 2$. The GITT indicates that LiV_2O_5 has the same equilibrium potential as LAGP, comparing Figures 1A and 1B, which was achieved by discharging the V_2O_5 at 0.05 C for 10 h followed by a rest of 100 h, as shown in Figure 1D. This means that when LiV_2O_5 and LAGP are mixed together, there is no difference in Li-chemical potential, and hence there is no driving force to establish a space-charge layer. To establish a difference in Li-chemical potential, V_2O_5 was discharged at 0.05 C to equilibrium potentials of 3.4 and 2.4 V versus Li/Li^+ corresponding to $\text{Li}_{0.2}\text{V}_2\text{O}_5$ and $\text{Li}_2\text{V}_2\text{O}_5$, respectively, as shown in Figures 1C and 1E. The potential difference or the equivalent difference in Li-chemical potential at the $\text{Li}_{0.2}\text{V}_2\text{O}_5$ -LAGP interface (0.4 V) and $\text{Li}_2\text{V}_2\text{O}_5$ -LAGP interface (0.6 V) will lead to the redistribution of Li-ions to equalize the electrochemical potential over the interface, hence establishing a space-charge layer.

Li-Ion Kinetics in Bulk $\text{Li}_{0.2}\text{V}_2\text{O}_5$, LiV_2O_5 , and $\text{Li}_2\text{V}_2\text{O}_5$

To prepare larger amounts of carbon black and binder-free $\text{Li}_x\text{V}_2\text{O}_5$ materials, as required for the detailed solid-state NMR studies, chemical lithiation was employed. Inductively coupled plasma (ICP) analysis of the prepared LiV_2O_5 , $\text{Li}_2\text{V}_2\text{O}_5$, and

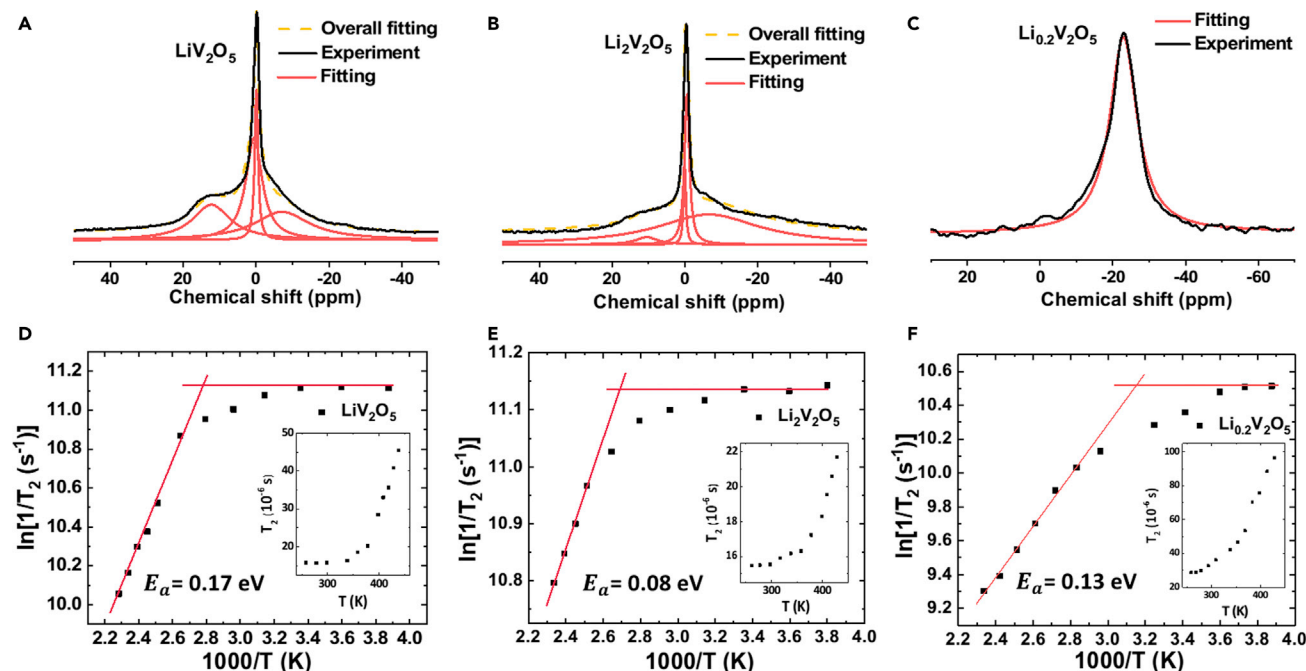


Figure 2. One-Dimensional NMR Characterizations of LiV_2O_5 , $\text{Li}_2\text{V}_2\text{O}_5$, and $\text{Li}_{0.2}\text{V}_2\text{O}_5$

(A–C) 1D ^6Li NMR spectrum of (A) LiV_2O_5 , (B) $\text{Li}_2\text{V}_2\text{O}_5$, and (C) $\text{Li}_{0.2}\text{V}_2\text{O}_5$.

(D–F) Arrhenius plot of the ^7Li spin-spin relaxation time T_2 for (D) LiV_2O_5 , (E) $\text{Li}_2\text{V}_2\text{O}_5$, and (F) $\text{Li}_{0.2}\text{V}_2\text{O}_5$.

$\text{Li}_{0.2}\text{V}_2\text{O}_5$ materials results in the expected Li content, as can be seen in Table S1. The XRD refinements, see Figure S2, show an increase in the c parameter with increased Li content in $\text{Li}_x\text{V}_2\text{O}_5$, indicating the puckering of the V_2O_5 layer.⁴⁰ To identify the Li-ion environment and kinetics in $\text{Li}_x\text{V}_2\text{O}_5$, one-dimensional (1D) ^6Li NMR was performed, the spectra of which are shown in Figures 2A–2C. As shown in Figures 2A and 2B, there are four different Li environments appearing at ~ 11 , 0.6, -0.3 , and -8 ppm. Based on previous neutron diffraction and ^7Li MAS (magic angle spinning) NMR results,⁴¹ the resonance around 11 ppm represents Li occupying the octahedral site, which is expected for $x < 1$ in $\text{Li}_x\text{V}_2\text{O}_5$, consistent with the decreased peak intensity at ~ 11 ppm in $\text{Li}_2\text{V}_2\text{O}_5$ compared with LiV_2O_5 . The resonance located at -8 ppm is assigned to the ϵ/δ -phase in LiV_2O_5 and $\text{Li}_2\text{V}_2\text{O}_5$, as reported previously.^{42,43} The other two resonances located near 0 ppm have been suggested to represent the Li environment in the γ -phase in LiV_2O_5 and $\text{Li}_2\text{V}_2\text{O}_5$, while other studies suggest that only one resonance near 0 ppm corresponds to the γ -phase.^{42,44,45} A possible explanation is that previous NMR studies of $\text{Li}_x\text{V}_2\text{O}_5$ were conducted using ^7Li ($I = 3/2$) NMR, having a lower resolution due to quadrupolar interactions, resulting in two resonances overlapping, as demonstrated in the ^7Li NMR MAS spectrum of LiV_2O_5 and $\text{Li}_2\text{V}_2\text{O}_5$ shown in Figure S3. In $\text{Li}_{0.2}\text{V}_2\text{O}_5$, there is only one broad resonance located around -24 ppm corresponding to the β -phase in low Li content $\text{Li}_x\text{V}_2\text{O}_5$.⁴²

To determine the Li-ion bulk diffusion kinetics of the compositions LiV_2O_5 , $\text{Li}_2\text{V}_2\text{O}_5$, and $\text{Li}_{0.2}\text{V}_2\text{O}_5$, spin-spin (T_2) relaxation NMR experiments were carried out at temperatures ranging from 258 to 438 K. In the analysis of the T_2 relaxation of LiV_2O_5 and $\text{Li}_2\text{V}_2\text{O}_5$, only the peak at -0.3 ppm was fitted as only this Li-ion environment appears to contribute to the Li-ion conductivity as discussed below. As can be seen in Figures 2D–2F, for all compositions the spin-spin relaxation rate, $1/T_2$,

remains constant until a specific temperature above which it increases with increasing temperature. The T_2 value at the “freezing” temperature range is related to the correlation time, τ_c , which is the lower limit of the average time for a Li-ion residing at one site before it hops to another site at that temperature.⁴⁶ The Bloembergen, Purcell, and Pound (BPP) model was applied to fit the spin-spin relaxation, as described in [Supplemental Information](#). [Figures 2D–2F](#) represents the Arrhenius plots for LiV_2O_5 , $\text{Li}_2\text{V}_2\text{O}_5$, and $\text{Li}_{0.2}\text{V}_2\text{O}_5$, resulting in activation energies of 0.17 ± 0.02 , 0.08 ± 0.01 , and 0.13 ± 0.01 eV for Li-ion in LiV_2O_5 , $\text{Li}_2\text{V}_2\text{O}_5$, and $\text{Li}_{0.2}\text{V}_2\text{O}_5$, respectively. The correlation times calculated via $\tau_c = T_2/\sqrt{2}$ from the break point between the low and mobility regime indicated by the crossing lines in [Figures 2D–2F](#) are 12.4 μs at ~ 360 K for LiV_2O_5 , 11.4 μs at ~ 373 K for $\text{Li}_2\text{V}_2\text{O}_5$, and 27.1 μs at ~ 317 K for $\text{Li}_{0.2}\text{V}_2\text{O}_5$. With these values, τ_∞ is computed to be 52, 950, and 230 ns, which leads to τ_c of 38.6, 21.3, and 36.2 μs at room temperature for LiV_2O_5 , $\text{Li}_2\text{V}_2\text{O}_5$, and $\text{Li}_{0.2}\text{V}_2\text{O}_5$, respectively. The microscopic diffusion coefficient at room temperature is usually determined with $D = l^2/n\tau_c$, where l is the length of an elementary jump between sites and n is the dimension factor. Assuming that the Li^+ diffusion in LiV_2O_5 is one dimensional along channels parallel to the b axis ([0 1 0] direction), Li^+ can jump from its octahedral site to two other equivalent sites, which leads to $n = 2$ and a jump distance equal to the b -lattice parameter.^{42,47} As a result, we could obtain 1.68×10^{-11} , 3.04×10^{-11} , and 1.79×10^{-11} $\text{cm}^2 \text{s}^{-1}$ for the diffusion coefficient at room temperature for LiV_2O_5 , $\text{Li}_2\text{V}_2\text{O}_5$, and $\text{Li}_{0.2}\text{V}_2\text{O}_5$, individually. These very similar diffusion coefficients indicate that the bulk-ion conductivity in these three phases is comparable.

Influence of Space-Charge Layers on the Li-Ion Transport

To investigate the Li-ion transport over the interfaces between $\text{Li}_x\text{V}_2\text{O}_5$ and LAGP, we prepared mixtures by hand grinding ball-milled $\text{Li}_x\text{V}_2\text{O}_5$ and LAGP powders, followed by pressing this mixture into a pellet under 100 MPa to establish contact between $\text{Li}_x\text{V}_2\text{O}_5$ and LAGP, representing the conditions in actual solid-state batteries. After this, the pellet was hand grinded in a mortar to enable filling the NMR rotor. Prior to the NMR experiments, the stability of the mixtures was investigated by conducting XRD and X-ray photoelectron spectroscopy (XPS) measurements. As observed in [Figures S4](#) and [S5](#), the results show no indication that $\text{Li}_x\text{V}_2\text{O}_5$ and LAGP react with each other, in line with the expected electrochemical stability window of LAGP³³ toward the potentials of the $\text{Li}_x\text{V}_2\text{O}_5$ $x = 0.2$ -2 compositions.

$1\text{D } ^6\text{Li}$ MAS NMR spectra of LiV_2O_5 -LAGP, $\text{Li}_2\text{V}_2\text{O}_5$ -LAGP, and $\text{Li}_{0.2}\text{V}_2\text{O}_5$ -LAGP mixtures are displayed in [Figures 3A](#), [3E](#), and [3I](#). In all three mixtures, the weight ratio between $\text{Li}_x\text{V}_2\text{O}_5$ and LAGP was set to 4:1. In [Figures 3A](#) and [3E](#) the two overlapping resonances around 0 ppm represent Li in LiV_2O_5 and $\text{Li}_2\text{V}_2\text{O}_5$, and the sharp resonance around -1.4 ppm represents the Li environment in LAGP. Note that the two additional broad resonances of LiV_2O_5 and $\text{Li}_2\text{V}_2\text{O}_5$, visible in [Figures 2A](#) and [2B](#), practically fade into the background due to their relative low intensity, as shown in [Figure S6](#). As expected, based on [Figure 2C](#), the $\text{Li}_{0.2}\text{V}_2\text{O}_5$ -LAGP mixture shown in [Figure 3I](#) results in the broad resonance of $\text{Li}_{0.2}\text{V}_2\text{O}_5$ at -24 ppm in addition to the sharp LAGP resonance at -1.4 ppm.

To investigate the impact of the presence of space-charge layers on the Li-ion transport kinetics over the $\text{Li}_x\text{V}_2\text{O}_5$ -LAGP interfaces, we conducted 2D exchange NMR measurements for the LiV_2O_5 -LAGP, $\text{Li}_2\text{V}_2\text{O}_5$ -LAGP, and $\text{Li}_{0.2}\text{V}_2\text{O}_5$ -LAGP mixtures. 2D exchange NMR offers the possibility to measure the spontaneous Li-ion exchange between different Li-ion environments, at present for the first time realized to study the impact of the space-charge layers between two solid phases. 2D

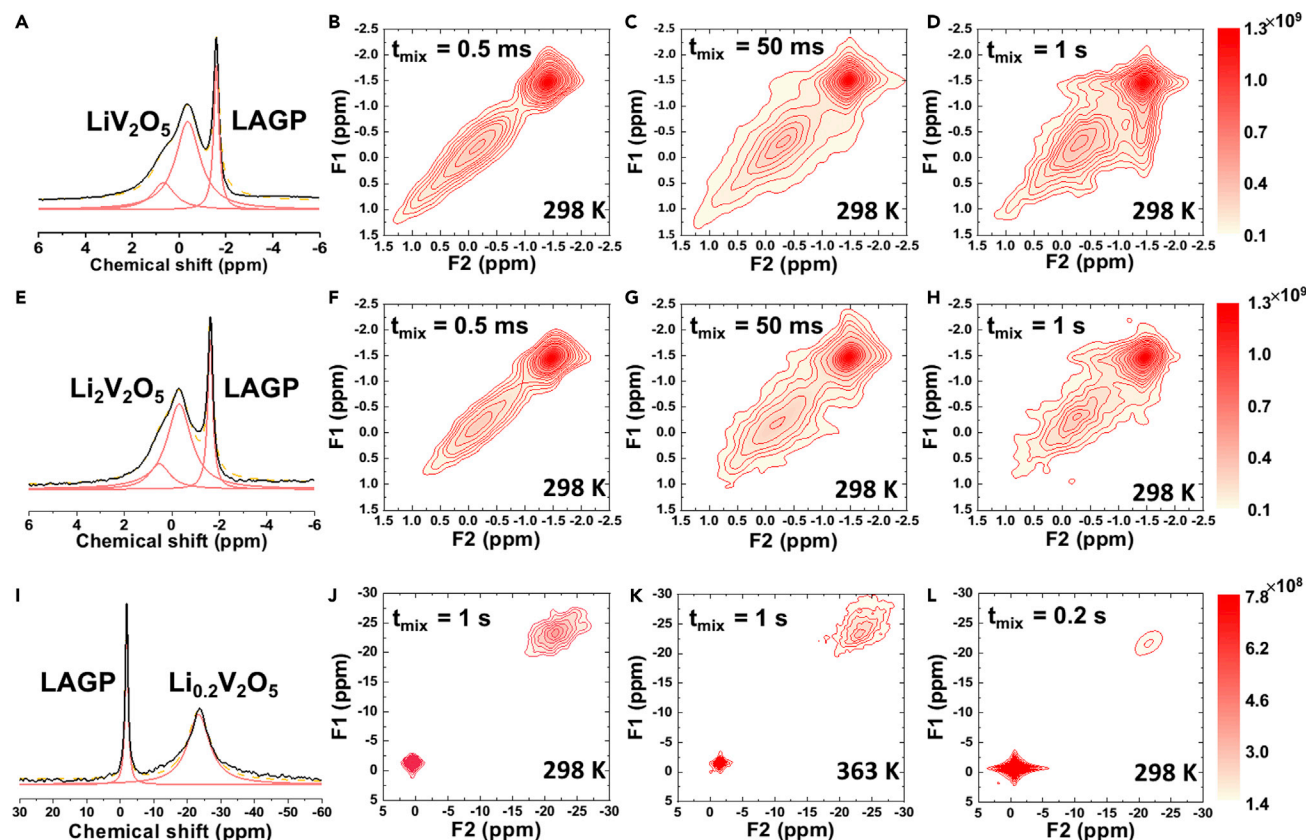


Figure 3. ^6Li NMR Exchange Experiments Quantifying the Spontaneous Lithium-Ion Transport between the $\text{Li}_x\text{V}_2\text{O}_5$ and LAGP

(A, E, and I) 1D ^6Li MAS spectrum corresponding to (A) the LiV_2O_5 -LAGP mixture, (E) the $\text{Li}_2\text{V}_2\text{O}_5$ -LAGP mixture, and (I) the $\text{Li}_{0.2}\text{V}_2\text{O}_5$ -LAGP mixture. (B–D) ^6Li 2D-EXSY spectrum of LiV_2O_5 -LAGP at room temperature for mixing time (B) 0.5 ms, (C) 50 ms, and (D) 1 s. (F–H) ^6Li 2D-EXSY spectrum of $\text{Li}_2\text{V}_2\text{O}_5$ -LAGP at room temperature for mixing time (F) 0.5 ms, (G) 50 ms, and (H) 1 s. (J) ^6Li 2D-EXSY spectrum of $\text{Li}_{0.2}\text{V}_2\text{O}_5$ -LAGP at room temperature for mixing time 1 s. (K) ^6Li 2D-EXSY spectrum of $\text{Li}_{0.2}\text{V}_2\text{O}_5$ -LAGP at 363 K for mixing time 1 s. (L) ^7Li 2D-EXSY spectrum of $\text{Li}_{0.2}\text{V}_2\text{O}_5$ -LAGP at room temperature for mixing time 0.2 s.

exchange NMR effectively records the spectrum of the ^6Li atoms at $t = 0$ s, allows a “mixing time” t_{mix} , subsequently recording the spectrum of the same ^6Li atoms again at $t = t_{\text{mix}}$. The results of these measurements are shown in Figure 3. The signal appearing on the diagonal reflects the 1D NMR spectrum in Figures 3A, 3E, and 3I, which represents ^6Li atoms having the same environment before and after t_{mix} . In contrast, the off-diagonal signal represents ^6Li atoms that have exchanged between the $\text{Li}_x\text{V}_2\text{O}_5$ and LAGP environments within the diffusion time t_{mix} . For a short mixing time of 0.5 ms (Figures 3B and 3F), there is virtually no Li-ion exchange and, thus, not sufficient Li-ions crossing the $\text{Li}_x\text{V}_2\text{O}_5$ -LAGP interface to be measured by the exchange experiments. For a much longer mixing time, $t_{\text{mix}} = 1$ s, clear cross peaks appear in the 2D exchange spectrum of both LiV_2O_5 -LAGP and $\text{Li}_2\text{V}_2\text{O}_5$ -LAGP mixtures. The weaker cross-peak intensity for the $\text{Li}_2\text{V}_2\text{O}_5$ -LAGP mixture implies significant less Li-ion exchange as compared with that in LiV_2O_5 -LAGP, as shown in Figures 3D and 3H. The stronger cross-peak intensity for the LiV_2O_5 -LAGP mixture signifies more facile Li-ion diffusion over the LiV_2O_5 -LAGP interface. For the $\text{Li}_{0.2}\text{V}_2\text{O}_5$ -LAGP mixture no cross peaks are observed at a long mixing time of $t_{\text{mix}} = 1$ s, Figure 3J, even at an elevated temperature of 363 K, Figure 3K, indicating that for this mixture the spontaneous Li transport between $\text{Li}_{0.2}\text{V}_2\text{O}_5$ and LAGP is the smallest. Note that the two resonances in LiV_2O_5 and $\text{Li}_2\text{V}_2\text{O}_5$ around 11 and -8 ppm

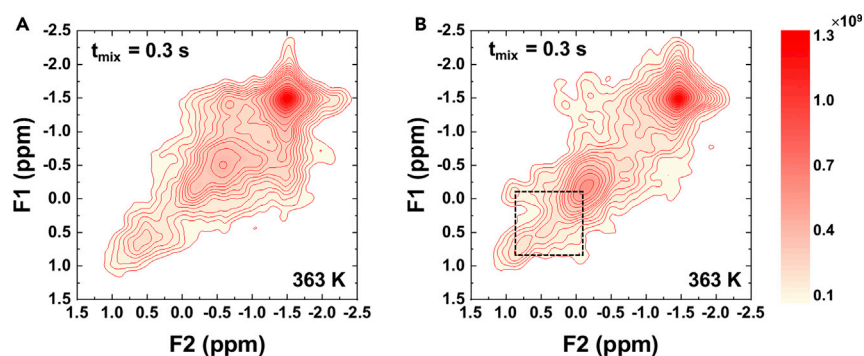


Figure 4. Exchange Phenomenon within LiV₂O₅ and Li₂V₂O₅ Bulk

(A and B) ^6Li 2D exchange NMR spectrum of (A) LiV₂O₅-LAGP and (B) Li₂V₂O₅-LAGP at 363 K with 0.3 s mixing time.

are invisible in the 2D exchange spectrum because of the relatively low intensity, as further illustrated by Figure S7. To further investigate the exchange in the Li_{0.2}V₂O₅-LAGP mixture, we conducted ^7Li NMR 2D experiments, raising the resonance intensities because of the higher natural abundance (^7Li 92.4% versus ^6Li 7.6%)⁴⁸ and the higher NMR sensitivity, however, at the expense of the lower resolution caused by the stronger dipolar interactions and presence of quadrupolar interactions. Despite the higher sensitivity on Li exchange, even this experiment did not result in measurable exchange, see Figure 3L. As the strongest Li exchange over the Li_xV₂O₅-LAGP interface is observed for the composition where the space-charge layer should be absent, $x = 1$, these results demonstrate that the space-charge layer, expected to be present for the compositions $x = 0.2$ and $x = 2$, hinders the spontaneous Li exchange.

More detailed evaluation of the 2D spectrum at 363 K brings forward another exchange phenomenon for the Li₂V₂O₅-LAGP mixture shown in Figure 4B, which is not present for the LiV₂O₅-LAGP mixture shown in Figure 4A. The off-diagonal intensity indicates exchange between Li-sites within Li₂V₂O₅ located at ~ 0.6 and -0.3 ppm, representing sites within the γ -phase. The different site occupation in Li₂V₂O₅ appears to boost the bulk diffusivity, also reflected by the higher diffusion coefficient as compared with LiV₂O₅ resulting from the T_2 relaxation experiments. Despite the higher bulk diffusivity in Li₂V₂O₅, the Li-ion exchange over the interface with the LAGP is significantly less as compared with LiV₂O₅, reflecting the large impact of the space-charge layer on the spontaneous Li-ion transport.

To quantify the exchange over the LiV₂O₅-LAGP and Li₂V₂O₅-LAGP interfaces, we carried out variable temperature ^6Li 2D exchange experiments. Quantification of the exchange between LiV₂O₅ (Li₂V₂O₅) and LAGP was performed by fitting the growing off-diagonal signal by a diffusion model derived from Fick's law, as described in Supplemental Information. The fitted results of the normalized cross-peak intensity as a function of mixing time for different temperatures are shown in Figure 5. By means of fitting the above demagnetization model, each temperature results in a diffusion coefficient, quantifying the activation energy for exchange between the Li_xV₂O₅ and LAGP phases, the results of which are shown in Figures 5A and 5C.

For the space-charge layer free LiV₂O₅-LAGP interface, the observed Li exchange at room temperature leads to an effective diffusion coefficient of approximately $1.0 \times 10^{-12} \text{ cm}^2 \text{ s}^{-1}$, see Figure S9, which is a factor of 17 times smaller than the

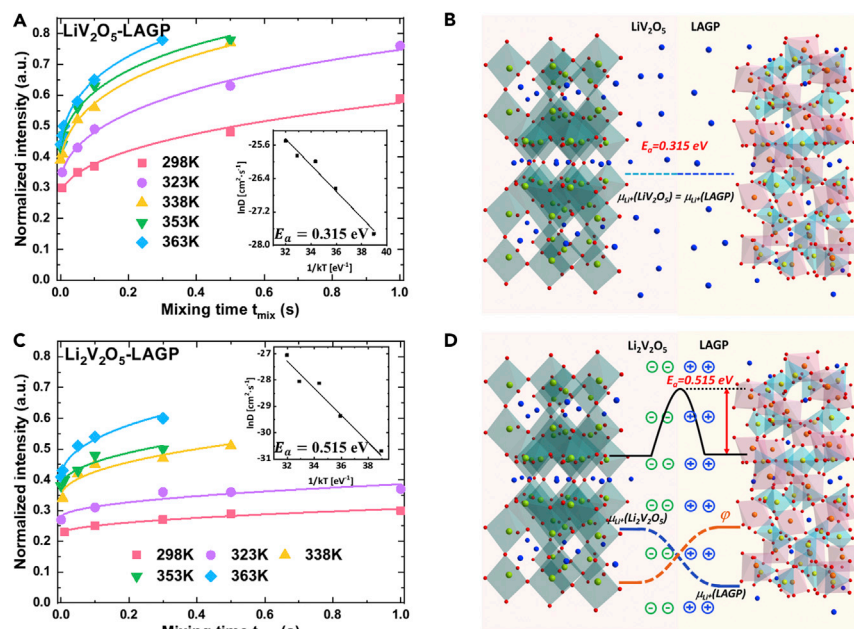


Figure 5. Determination of the Activation Energy of Li-Ion Exchange and Schematic of Space-Charge Layer Effects on Li-Ion Transport

(A and C) Normalized intensity of the cross peaks in ^6Li exchange NMR spectrum as a function of mixing time at different temperatures for (A) LiV_2O_5 -LAGP and (C) $\text{Li}_2\text{V}_2\text{O}_5$ -LAGP. The insets show the temperature dependence of the diffusion parameter D based on the Arrhenius law. (B and D) Schematic representation of the impact of the space-charge layer at the interface of (B) LiV_2O_5 -LAGP and (D) $\text{Li}_2\text{V}_2\text{O}_5$ -LAGP. The blue atoms represent the lithium-ion.

bulk diffusion coefficient as determined by T_2 relaxation. Additionally, the activation energy for diffusion over the interface, 315 meV, is much larger than that for bulk diffusion, amounting 170 meV from the T_2 relaxation experiments in Figure 2D. This most likely indicates that the grain boundary between space-charge free LiV_2O_5 -LAGP offers restricted contact points as well as introducing an additional diffusional barriers,^{36,49} as also suggested by the electrochemical impedance spectroscopy (EIS) measurement of the LiV_2O_5 -LAGP mixtures in Figure S8, reflecting one of the main challenges to achieve high performance ASSBs.

Driven by the 0.6 V difference in Li-chemical potential, introduction of the space-charge layer at the $\text{Li}_2\text{V}_2\text{O}_5$ -LAGP interface increases the resistance of the interface against charge transport significantly. The effective diffusion coefficient drops to $4.4 \times 10^{-14} \text{ cm}^2 \text{ s}^{-1}$, as shown in Figure S9, more than 20 times smaller compared with the space-charge free LiV_2O_5 -LAGP interface and the activation energy for exchange raises to 515 meV. The decreased Li-ion exchange must be due to the presence of the space-charge layer because the diffusivity of the bulk LAGP is the same for all three systems, amounting $\sim 10^{-13} \text{ cm}^2 \text{ s}^{-1}$ and 166 meV,⁵⁰ and because the bulk diffusivity of the three $\text{Li}_x\text{V}_2\text{O}_5$ phases is comparable, as determined by the T_2 relaxation experiments ($x = 0.2$: 1.79×10^{-11} , $x = 1$: 1.68×10^{-11} , and $x = 2$: $3.04 \times 10^{-11} \text{ cm}^2 \text{ s}^{-1}$). As schematically shown in Figures 5B and 5D, the space-charge layer poses an additional barrier, on top of that posed by the grain boundary, that hinders the Li-ion transport over the electrode-electrolyte interface.

Because the NMR exchange experiments are performed under equilibrium conditions, it provides a direct quantitative measurement of the exchange current density

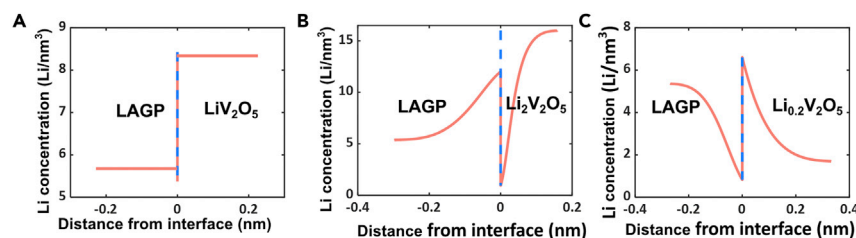


Figure 6. Space-Charge Layer Model Calculation of LiV_2O_5 -LAGP, $\text{Li}_2\text{V}_2\text{O}_5$ -LAGP, and $\text{Li}_{0.2}\text{V}_2\text{O}_5$ -LAGP Interfaces

(A–C) lithium concentration at the (A) LiV_2O_5 -LAGP interface, (B) $\text{Li}_2\text{V}_2\text{O}_5$ -LAGP interface and (C) $\text{Li}_{0.2}\text{V}_2\text{O}_5$ -LAGP interface.

over the electrode-electrolyte interface, thus reflecting the intrinsic mobility of the Li-ions over the interface. During the same mixing time of 1 s at room temperature, about 57% of the total amount of Li-ions exchanged over the LiV_2O_5 -LAGP interface, while for $\text{Li}_2\text{V}_2\text{O}_5$ -LAGP, only 30% Li-ion exchanged as shown in Figures 5A and 5C. From the amount of the exchanged Li-ion, and taking into consideration the average crystallite sizes of $\text{Li}_x\text{V}_2\text{O}_5$ and LAGP, we obtain the room temperature exchange current density, which is deemed as one of the critical parameters that will determine the maximum power of a battery, amounting 0.77 mA cm^{-2} for space-charge-layer-free LiV_2O_5 -LAGP and 0.41 mA cm^{-2} in the presence of the space-charge layer in $\text{Li}_2\text{V}_2\text{O}_5$ -LAGP. To estimate the maximum exchange current density over the $\text{Li}_{0.2}\text{V}_2\text{O}_5$ -LAGP, where no exchange is observed, we assume that the exchange is at most in the order of the background signal, resulting in a maximum exchange current density of 0.13 mA cm^{-2} over the $\text{Li}_{0.2}\text{V}_2\text{O}_5$ -LAGP interface. The larger exchange current density for LiV_2O_5 -LAGP as compared with the $\text{Li}_2\text{V}_2\text{O}_5$ -LAGP and $\text{Li}_{0.2}\text{V}_2\text{O}_5$ -LAGP interfaces further demonstrates that the space-charge layer hinders the Li-ion exchange over the interface significantly. For comparison, the exchange current density at typical electrode-liquid electrolyte interfaces in Li-ion batteries exceeds 1 mA cm^{-2} ,^{51,52} underlining that the solid-solid interfaces limit the power density of ASSBs.

To gain more insight in the role of the space-charge layers, we applied the space-charge layer model from our previous work⁵³ to the $\text{Li}_x\text{V}_2\text{O}_5$ -LAGP interfaces. Assuming that only ions are mobile and the interface is chemically stable with perfect contact, by using a solid solution model the chemical potential as a function of the distance near the interface can be determined from the corresponding ion concentration, where the law of mass conservation serves as the boundary condition. Specially, the Coulombic interaction between defects was taken into account, as proposed by Maier and co-workers,^{54,55} which is essential to approximate the formation energy of vacancies. This model does not take into account the electron (hole) transfer through band bending at the cathode-solid electrolyte interface, which can have a large impact on the space-charge formation, as recently predicted for the $\text{LiPON-Li}_x\text{CoO}_2$ by Swift and Qi.⁵⁶ Because of the large bandgap of $\text{Li}_x\text{V}_2\text{O}_5$ ⁵⁷ and its position relative to the bandgap to that of LAGP,⁵⁸ the valence band maxima are far apart, unlike at the $\text{LiPON-Li}_x\text{CoO}_2$ interface.⁵⁹ As a consequence, it should be expected that band bending has less impact on the space-charge formation in the present system, suggesting that the current model is a good approximation for the investigated interfaces. The parameters to perform the space-charge model calculations are listed in Table S2. The voltages of LAGP, LiV_2O_5 , $\text{Li}_2\text{V}_2\text{O}_5$, and $\text{Li}_{0.2}\text{V}_2\text{O}_5$ are set to be 3, 3, 2.4, and 3.4 V, respectively, which is based on the electrochemical measurements in Figure 1. As displayed in Figures 6B and 6C, in

$\text{Li}_2\text{V}_2\text{O}_5$ -LAGP and $\text{Li}_{0.2}\text{V}_2\text{O}_5$ -LAGP, the difference in potential between electrode and solid electrolyte, reflects the difference in Li-chemical potential, which results in the redistribution of the Li-ion concentration at the interface to equalize the electrochemical potential. This represents the formation of the space-charge layer having a ~ 0.5 nm thickness for $\text{Li}_2\text{V}_2\text{O}_5$ -LAGP and ~ 0.7 nm for the $\text{Li}_{0.2}\text{V}_2\text{O}_5$ -LAGP interface. This indicates that space charges occur over only a few atomic layers adjacent to the interfaces. Only taking the changes in Li concentration into account, the resistance because of the space-charge layers for $\text{Li}_2\text{V}_2\text{O}_5$ -LAGP and $\text{Li}_{0.2}\text{V}_2\text{O}_5$ -LAGP are very small, amounting to 0.0009 and $0.0061 \Omega \text{ cm}^2$, respectively (see Figure S10). It should be noted that the predicted large local depletion in LAGP at the $\text{Li}_{0.2}\text{V}_2\text{O}_5$ -LAGP interface may lead to the LAGP structure to collapse at the interfaces, potentially posing an additional barrier for Li-ion transport.

From the measured exchange current density, the interface resistance can be determined based on the relationship given by G. Horvai.⁶⁰ The resulting interface resistances are approximately $33 \Omega \text{ cm}^2$ for space-charge layer free LiV_2O_5 -LAGP increasing to $63 \Omega \text{ cm}^2$ for $\text{Li}_2\text{V}_2\text{O}_5$ -LAGP and $188 \Omega \text{ cm}^2$ for $\text{Li}_{0.2}\text{V}_2\text{O}_5$ -LAGP. These values are five orders of magnitude larger as compared with that from the space-charge layer calculations. The model calculations only approximately take into account the impact of the composition on the diffusion coefficient and not the effect of the grain boundary resistance that is anticipated to exist between the electrolyte and electrode particles⁴⁹ (see also Figure S8) and also not the charge dipole due to the space-charge layer.⁵⁶ Based on this, it is concluded that the impact of the changes in Li-ion concentrations in the space-charge layers have a negligible effect on the interface resistance as compared with the grain boundary resistance, suggesting that the charge separation of the space-charge layer is responsible for the significant increase in the interface resistance. For the present electrolyte-electrode combination, the space-charge layer is demonstrated to add more than $100 \Omega \text{ cm}^2$ to the interface resistance. For LAGP assuming a conductivity of $10^{-3} \text{ S cm}^{-1}$, the corresponding resistance for a $100 \mu\text{m}$ thick solid electrolyte is $10 \Omega \text{ cm}^2$, demonstrating the potentially large contributions of space-charge layers to the internal resistance of ASSBs, depending on the electrode and electrolyte geometry. Clearly, the resistance due to the space-charge layer will strongly vary depending on the electrode potential, in the present case depending on the $\text{Li}_x\text{V}_2\text{O}_5$ composition, and thus on the state of charge. Moreover, also the kinetic polarization of the electrode during high rate cycling can be expected to affect the space-charge layer, depending on the detailed resistances toward both Li-ion and electron charge carriers.

Conclusion and Outlook

Using $\text{Li}_x\text{V}_2\text{O}_5$ -LAGP as model system, the present NMR measurements and model calculations demonstrate the important role of space-charge layers at the cathode-solid electrolyte interface. The Li-ion transport kinetics from cathode to solid electrolyte (and vice versa) can be directly measured by 2D NMR exchange experiments, a direct probe of the exchange current density. For the LiV_2O_5 -LAGP interface, where there is no space-charge layer based on the equal Li-chemical potential, the activation energy for Li exchange and the resistance toward Li-ion transport is found to be significantly smaller than that in $\text{Li}_2\text{V}_2\text{O}_5$ -LAGP, where the difference in Li-chemical potential results in a space-charge layer at the interface. Consistently, the exchange current density directly measured by the NMR exchange experiments drops with the presence of the space-charge layer, providing direct insight in the interface resistance posed by the charge distribution as a consequence of the space-charge layer. Thereby, this work reveals the quantitative impact of the space-charge layers on the cathode-solid electrolyte interface in ASSBs, pointing out the importance of

strategies to mitigate the space-charge layer effects, for instance by reducing the local chemical potential difference at the cathode-solid electrolyte interface.

EXPERIMENTAL PROCEDURES

Resource Availability

Lead Contact

Further information and requests for resources and materials should be directed to and will be fulfilled by the Lead Contact, Marnix Wagemaker (m.wagemaker@tudelft.nl).

Materials Availability

The materials generated in this study will be made available on reasonable request.

Data and Code Availability

Supporting data and code of this study will be made available on reasonable request.

Full details of all experiments and materials are provided in [Supplemental Experimental Procedures](#).

SUPPLEMENTAL INFORMATION

Supplemental Information can be found online at <https://doi.org/10.1016/j.joule.2020.04.002>.

ACKNOWLEDGMENTS

The authors thank Frans Ooms for the assistance with experiments. This research was partially supported by the National Key Research and Development Program of China (2016YFB0100203), the National Natural Science Foundation of China (21922508, 21673116, 21633003, and U1801251), the Natural Science Foundation of Jiangsu Province of China (BK20190009), and the PAPD of Jiangsu Higher Education Institutions. The authors acknowledge support by the Netherlands Organization for Scientific Research (NWO) under the grant number. 15788 and M.W. under the VICI grant number. 16122. Financial support from the Advanced Dutch Energy Materials (ADEM) program of the Dutch Ministry of Economic Affairs, Agriculture, and Innovation is gratefully acknowledged. Financial support from the Chinese Scholarship Council (CSC) is gratefully acknowledged.

AUTHOR CONTRIBUTIONS

M.W., H.Z., and P.H. conceived and designed the project. Z.C., S.G., and M.L. performed the NMR experiments. C.L. provided the samples. M.L. helped with the XRD and XPS experiments, and Z.L. helped with the XRD refinements. Z.C. and S.G. analyzed experiment results, with contributions from X.Z. and P.H. to scientific discussion. Z.C. and M.W. wrote the manuscript. Z.C. and M.L. contributed equally to the work. All the authors helped in writing the manuscript.

DECLARATION OF INTERESTS

The authors declare no competing interests.

Received: December 17, 2019

Revised: January 22, 2020

Accepted: April 3, 2020

Published: May 7, 2020

REFERENCES

- Goodenough, J.B., and Park, K.S. (2013). The Li-ion rechargeable battery: a perspective. *J. Am. Chem. Soc.* **135**, 1167–1176.
- He, P., Yu, H., Li, D., and Zhou, H. (2012). Layered lithium transition metal oxide cathodes towards high energy lithium-ion batteries. *J. Mater. Chem.* **22**, 3680–3695.
- Ganapathy, S., and Wagemaker, M. (2012). Nanosize storage properties in spinel $\text{Li}_4\text{Ti}_5\text{O}_{12}$ explained by anisotropic surface lithium insertion. *ACS Nano* **6**, 8702–8712.
- Xu, K. (2004). Nonaqueous liquid electrolytes for lithium-based rechargeable batteries. *Chem. Rev.* **104**, 4303–4417.
- Liu, X., Peng, S., Gao, S., Cao, Y., You, Q., Zhou, L., Jin, Y., Liu, Z., and Liu, J. (2018). Electric-field-directed parallel alignment architecting 3D lithium-ion pathways within solid composite electrolyte. *ACS Appl. Mater. Interfaces* **10**, 15691–15696.
- Lotsch, B.V., and Maier, J. (2017). Relevance of solid electrolytes for lithium-based batteries: a realistic view. *J. Electroceram.* **38**, 128–141.
- Takada, K. (2013). Progress and prospective of solid-state lithium batteries. *Acta Mater.* **61**, 759–770.
- Wang, C., Xie, H., Zhang, L., Gong, Y., Pastel, G., Dai, J., Liu, B., Wachsmann, E.D., and Hu, L. (2018). Universal soldering of lithium and sodium alloys on various substrates for batteries. *Adv. Energy Mater.* **8**, 1–8.
- Han, X., Gong, Y., Fu, K.K., He, X., Hitz, G.T., Dai, J., Pearce, A., Liu, B., Wang, H., Rubloff, G., et al. (2017). Negating interfacial impedance in garnet-based solid-state Li metal batteries. *Nat. Mater.* **16**, 572–579.
- Bae, J., Li, Y., Zhang, J., Zhou, X., Zhao, F., Shi, Y., Goodenough, J.B., and Yu, G. (2018). A 3D nanostructured hydrogel-framework-derived high-performance composite polymer lithium-ion electrolyte. *Angew. Chem. Int. Ed.* **57**, 2096–2100.
- Kamaya, N., Homma, K., Yamakawa, Y., Hirayama, M., Kanno, R., Yonemura, M., Kamiyama, T., Kato, Y., Hama, S., Kawamoto, K., and Mitsui, A. (2011). A lithium superionic conductor. *Nat. Mater.* **10**, 682–686.
- Deiseroth, H.J., Kong, S.T., Eckert, H., Vannahme, J., Reiner, C., Zaiss, T., and Schlosser, M. (2008). $\text{Li}_6\text{PS}_5\text{X}$: a class of crystalline Li-rich solids with an unusually high Li^+ mobility. *Angew. Chem. Int. Ed.* **47**, 755–758.
- Kim, S., Oguchi, H., Toyama, N., Sato, T., Takagi, S., Otomo, T., Arunkumar, D., Kuwata, N., Kawamura, J., and Orimo, S.I. (2019). A complex hydride lithium superionic conductor for high-energy-density all-solid-state lithium metal batteries. *Nat. Commun.* **10**, 1081.
- Xu, L., Tang, S., Cheng, Y., Wang, K., Liang, J., Liu, C., Cao, Y.-C., Wei, F., and Mai, L. (2018). Interfaces in solid-state lithium batteries. *Joule* **2**, 1991–2015.
- Zhang, Z., Shao, Y., Lotsch, B., Hu, Y.S., Li, H., Janek, J., Nazar, L.F., Nan, C.W., Maier, J., Armand, M., and Chen, L. (2018). New horizons for inorganic solid state ion conductors. *Energy Environ. Sci.* **11**, 1945–1976.
- Janek, J., and Zeier, W.G. (2016). A solid future for battery development. *Nat. Energy* **1**, 16141.
- Yu, X., and Manthiram, A. (2018). Electrode-electrolyte interfaces in lithium-based batteries. *Energy Environ. Sci.* **11**, 527–543.
- Takada, K., Ohta, N., Zhang, L., Xu, X., Hang, B.T., Ohnishi, T., Osada, M., and Sasaki, T. (2012). Interfacial phenomena in solid-state lithium battery with sulfide solid electrolyte. *Solid State Ionics* **225**, 594–597.
- Takada, K., Ohno, T., Ohta, N., Ohnishi, T., and Tanaka, Y. (2018). Positive and negative aspects of interfaces in solid-state batteries. *ACS Energy Lett.* **3**, 98–103.
- Takada, K., Ohta, N., and Tateyama, Y. (2015). Recent progress in interfacial nanoarchitectonics in solid-state batteries. *J. Inorg. Organomet. Polym. Mater.* **25**, 205–213.
- Maier, J. (1987). Defect chemistry and conductivity effects in heterogeneous solid electrolytes. *J. Electrochem. Soc.* **134**, 1524.
- Maier, J. (1984). Enhancement of the ionic conductivity in solid-solid-dispersions by surface induced defects. *Berichte der Bunsengesellschaft für physikalische Chemie* **88**, 1057–1062.
- Maier, J. (2005). Nanoionics: ion transport and electrochemical storage in confined systems. *Nat. Mater.* **4**, 805–815.
- Yamada, H., Suzuki, K., Oga, Y., Saruwatari, I., and Moriguchi, I. (2013). Lithium depletion in the solid electrolyte adjacent to cathode materials. *ECS Trans.* **50**, 1–12.
- Luntz, A.C., Voss, J., and Reuter, K. (2015). Interfacial challenges in solid-state Li ion batteries. *J. Phys. Chem. Lett.* **6**, 4599–4604.
- Takada, K. (2018). Progress in solid electrolytes toward realizing solid-state lithium batteries. *J. Power Sources* **394**, 74–85.
- Goodyer, C.E., Fish, J.S., Fehribach, J.D., O'Hayre, R., and Bunge, A.L. (2011). Modeling space charge layer interaction and conductivity enhancement in nanoionic composites. *Electrochim. Acta* **56**, 9295–9302.
- Okumura, T., Nakatsutsumi, T., Ina, T., Orikasa, Y., Arai, H., Fukutsuka, T., Iriyama, Y., Uruga, T., Tanida, H., Uchimoto, Y., and Ogumi, Z. (2011). Depth-resolved X-ray absorption spectroscopic study on nanoscale observation of the electrode-solid electrolyte interface for all solid state lithium ion batteries. *J. Mater. Chem.* **21**, 10051–10060.
- Brogioli, D., Langer, F., Kun, R., and La Mantia, F. (2019). Space-charge effects at the $\text{Li}_7\text{La}_3\text{Zr}_2\text{O}_{12}$ /Poly(ethylene oxide) interface. *ACS Appl. Mater. Interfaces* **11**, 11999–12007.
- Cocciantelli, J.M., Ménétrier, M., Delmas, C., Doumerc, J.P., Pouchard, M., Broussely, M., and Labat, J. (1995). On the $\delta \rightarrow \gamma$ irreversible transformation in $\text{Li}/\text{V}_2\text{O}_5$ secondary batteries. *Solid State Ionics* **78**, 143–150.
- Liu, J., Zhou, Y., Wang, J., Pan, Y., and Xue, D. (2011). Template-free solvothermal synthesis of yolk-shell V_2O_5 microspheres as cathode materials for Li-ion batteries. *Chem. Commun.* **47**, 10380–10382.
- Pan, A., Wu, H.B., Yu, L., Zhu, T., and Lou, X.W. (2012). Synthesis of hierarchical three-dimensional vanadium oxide microstructures as high-capacity cathode materials for lithium-ion batteries. *ACS Appl. Mater. Interfaces* **4**, 3874–3879.
- Xu, X., Wen, Z., Wu, X., Yang, X., and Gu, Z. (2007). Lithium ion-conducting glass-ceramics of $\text{Li}_{1.5}\text{Al}_{0.5}\text{Ge}_{1.5}(\text{PO}_4)_3-x\text{Li}_2\text{O}$ ($x=0.0-0.20$) with good electrical and electrochemical properties. *J. Am. Ceram. Soc.* **90**, 2802–2806.
- Wagemaker, M., Kentgens, A.P.M., and Mulder, F.M. (2002). Equilibrium lithium transport between nanocrystalline phases in intercalated TiO_2 anatase. *Nature* **418**, 397–399.
- Ganapathy, S., van Eck, E.R., Kentgens, A.P., Mulder, F.M., and Wagemaker, M. (2011). Equilibrium lithium-ion transport between nanocrystalline lithium-inserted anatase TiO_2 and the electrolyte. *Chemistry* **17**, 14811–14816.
- Yu, C., Ganapathy, S., Eck, E.R.H.V., Wang, H., Basak, S., Li, Z., and Wagemaker, M. (2017). Accessing the bottleneck in all-solid state batteries, lithium-ion transport over the solid-electrolyte-electrode interface. *Nat. Commun.* **8**, 1086.
- Liu, Y., Li, B., Kitaura, H., Zhang, X., Han, M., He, P., and Zhou, H. (2015). Fabrication and performance of all-solid-state Li-Air battery with SWCNTs/LAGP cathode. *ACS Appl. Mater. Interfaces* **7**, 17307–17310.
- Feng, J.K., Lu, L., and Lai, M.O. (2010). Lithium storage capability of lithium ion conductor $\text{Li}_{1.5}\text{Al}_{0.5}\text{Ge}_{1.5}(\text{PO}_4)_3$. *J. Alloys Compd.* **501**, 255–258.
- Li, W.-D., Xu, C.-Y., Du, Y., Fang, H.-T., Feng, Y.-J., and Zhen, L. (2014). Electrochemical lithium insertion behavior of $\beta\text{-Li}_x\text{V}_2\text{O}_5$ ($0 < x \leq 3$) as the cathode material for secondary lithium batteries. *J. Electrochem. Soc.* **161**, A75–A83.
- Galy, J. (1992). Vanadium pentoxide and vanadium oxide bronzes—structural chemistry of single (S) and double (D) layer $\text{M}_x\text{V}_2\text{O}_5$ phases. *J. Solid State Chem.* **100**, 229–245.
- Cocciantelli, J.M., Suh, K.S., Sénégas, J., Doumerc, J.P., Soubeyroux, J.L., Pouchard, M., and Hagemuller, P. (1992). ^7Li NMR in electrochemically intercalated $\gamma\text{-Li}_x\text{V}_2\text{O}_5$ bronzes ($0.95 \leq x \leq 1.9$). *J. Phys. Chem. Solids* **53**, 51–55.
- Nishioka, D., Nakamura, K., Michihiro, Y., Ohno, T., Vijayakumar, M., Selvasekarapandian, S., and Deguchi, H. (2008). NMR study on Li^+ ionic motion in $\text{Li}_x\text{V}_2\text{O}_5$ ($0.4 \leq x \leq 1.4$). *J. Phys. Soc. Jpn.* **77**, 024602.
- Grey, C.P., and Dupré, N. (2004). NMR studies of cathode materials for lithium-ion

- rechargeable batteries. *Chem. Rev.* **104**, 4493–4512.
44. Vijayakumar, M., Selvasekarapandian, S., Nakamura, K., Kanashiro, T., and Kesavamoorthy, R. (2004). ^7Li MAS-NMR and vibrational spectroscopic investigations of $\text{Li}_x\text{V}_2\text{O}_5$ ($x=1.0, 1.2$ and 1.4). *Solid State Ionics* **167**, 41–47.
45. Stallworth, P.E., Johnson, F.S., Greenbaum, S.G., Passerini, S., Flowers, J., and Smyrl, W. (2002). Magnetic resonance studies of chemically intercalated $\text{Li}_x\text{V}_2\text{O}_5$ aerogels. *J. Appl. Phys.* **92**, 3839–3852.
46. Wagemaker, M., Van De Krol, R., Kentgens, A.P.M., Van Well, A.A., and Mulder, F.M. (2001). Two phase morphology limits lithium diffusion in TiO_2 (anatase): a ^7Li MAS NMR study. *J. Am. Chem. Soc.* **123**, 11454–11461.
47. Cocciantelli, J.M., Suh, K.S., Senegas, J., Doumerc, J.P., and Pouchard, M. (1992). ^7Li NMR of electrochemically inserted $\text{Li}_x\text{V}_2\text{O}_5$. *J. Phys. Chem. Solids* **53**, 57–59.
48. Liu, H., Choe, M.J., Enrique, R.A., Orvañanos, B., Zhou, L., Liu, T., Thornton, K., and Grey, C.P. (2017). Effects of antisite defects on Li diffusion in LiFePO_4 revealed by Li isotope exchange. *J. Phys. Chem. C* **121**, 12025–12036.
49. Famprikis, T., Canepa, P., Dawson, J.A., Islam, M.S., and Masquelier, C. (2019). Fundamentals of inorganic solid-state electrolytes for batteries. *Nat. Mater.* **18**, 1278–1291.
50. Hayamizu, K., and Seki, S. (2017). Long-range Li ion diffusion in NASICON-type $\text{Li}_{1.5}\text{Al}_{0.5}\text{Ge}_{1.5}(\text{PO}_4)_3$ (LAGP) studied by ^7Li pulsed-gradient spin-echo NMR. *Phys. Chem. Chem. Phys.* **19**, 23483–23491.
51. Doyle, M., and Newman, J. (1997). Analysis of capacity-rate data for lithium batteries using simplified models of the discharge process. *J. Appl. Electrochem.* **27**, 846–856.
52. Guo, P., Song, H., and Chen, X. (2009). Electrochemical performance of graphene nanosheets as anode material for lithium-ion batteries. *Electrochem. Commun.* **11**, 1320–1324.
53. de Klerk, N.J.J., and Wagemaker, M. (2018). Space-charge layers in all-solid-state batteries; Important or Negligible? *ACS Appl. Energy Mater.* **1**, 5609–5618.
54. Maier, J. (2005). Chemical potential of charge carriers in solids. *Z. Phys. Chem.* **219**, 35–46.
55. Hainovsky, N., and Maier, J. (1995). Simple phenomenological approach to premelting and sublattice melting in Frenkel disordered ionic crystals. *Phys. Rev. B Condens. Matter* **51**, 15789–15797.
56. Swift, M.W., and Qi, Y. (2019). First-Principles prediction of potentials and space-charge layers in all-solid-state batteries. *Phys. Rev. Lett.* **122**, 167701.
57. Li, Z.Y., and Wu, Q.H. (2008). Electronic structures of $\text{Li}_x\text{V}_2\text{O}_5$ ($x=0.5$ and 1): a theoretical study. *ChemPhysChem* **9**, 300–304.
58. Schwietert, T.K., Arszewska, V.A., Wang, C., Yu, C., Vasileiadis, A., de Klerk, N.J.J., Hageman, J., Hupfer, T., Kerkamm, I., Xu, Y., et al. (2020). Clarifying the relationship between redox activity and electrochemical stability in solid electrolytes. *Nat. Mater.* **19**, 428–435.
59. Milewska, A., Świerczek, K., Tobola, J., Boudoire, F., Hu, Y., Bora, D.K., Mun, B.S., Braun, A., and Molenda, J. (2014). The nature of the nonmetal–metal transition in Li_xCoO_2 oxide. *Solid State Ionics* **263**, 110–118.
60. Horvai, G. (1991). Relationship between charge transfer resistance and exchange current density of ion transfer at the interface of two immiscible electrolyte solutions. *Electroanalysis* **3**, 673–675.